Effects of charge screening and surface properties on signal transduction in field effect nanowire biosensors

Yang Liu[a] and Robert W. Dutton
Center for Integrated Systems, Stanford University, Stanford, California 94305-4075, USA

(Received 5 February 2009; accepted 23 May 2009; published online 6 July 2009)

A self-consistent numerical model for silicon-based field effect nanowire biosensors is developed to study the impact of various surface-related physical and chemical processes, including transport of semiconductor carriers and electrolyte mobile ions, protonation and deprotonation of surface charge groups, and charges, and orientations and surface binding dynamics of immobilized biomolecules. It is shown that the sensing signal levels are affected by the gate biasing points, nonlinear screening from both electrolytes and surface charge groups, as well as the biomolecule charges and orientations. The critical role of the nanowire surface heterogeneity in determining the sensing input dynamic range is indicated based on correlations with experimental data. © *2009 American Institute of Physics*. [DOI: 10.1063/1.3156657]

I. INTRODUCTION

Ion-sensitive field effect transistor-type devices[1] have been explored for direct detection of biomolecular charges more than a decade ago.[2] More recently, substantial research interests in this field have been focused on the demonstrations of silicon nanowire (Si-NW) biosensors for electrical detection of DNA hybridization[3–7] and immunological antibody/antigen interactions.[8–10] The signal transduction mechanism is based on field effect: functionalized NW surfaces are immobilized with receptor layers (primary ssDNAs or antibodies); upon the specific binding of the analytes [complementary ssDNAs (*c*-DNAs) or antigens], the biological charges carried by the analytes modulate NW surface potentials and consequently change the electrical conductance. Such electrical-based, label-free biosensing devices promise important applications in both life science instrumentation and for low-cost medical diagnostics. The performance of Si-NW biosensors depends on complex, surface-related physical and chemical processes involving biological charges, semiconductor carriers, electrolyte ions, surface charge groups, as well as biomolecule surface binding dynamics. Indeed, a large range of measured signals have been reported: 10%–200% in relative conductance changes and two to four orders of magnitude in input dynamic range, taking DNA sensing as an example.[3–7] This strongly suggests the need of quantitative models for better understanding of the device physics and in support of rational device design.

Several modeling efforts for Si-NW biosensors have been previously reported;[11–13] however, self-consistent treatments of the various physical and chemical processes involved in signal transduction are still lacking. Our previous modeling work has studied the effect of electrodiffusion on electrolyte screening in both nanopores[14] and NWs,[15] where only a single biomolecule was considered in a three-dimensional setting. In this work, a fast, self-consistent numerical model is developed at the device level to clarify the roles of various processes including semiconductor carrier transport, electrolyte screening, protonation and deprotonation of surface charge groups, and binding dynamics between surface-bound analyte biomolecules and those in solutions. The modeling approach follows that of Ref. 16, where the ensemble of surface-bound oligomers is modeled as a layer of charged, ion-permeable membrane. The major improvements of this work over Ref. 16 include the modeling of semiconductor carriers, treatment of both amphoteric (amine) and basic (hydroxyl) surface charge groups,[17] and the membrane partition effect.[18] Additionally, the geometrical difference between the planar structures and cylindrical NW structures used in this work is significant. Consideration of the partition effect is necessary in the case of high surface density of the immobilized DNA oligomers ($>\sim 10^{13}/\mathrm{cm}^2$ as measured in Ref. 6). While initial results of this work have been reported in Ref. 19, this paper provides an in-depth treatment of device physics.

The numerical modeling approach is presented in Sec. II, together with description of the underlying device physics. In Sec. III, the numerical model is used to examine the roles of important biosensing parameters, including gate biasing points, DNA surface densities and orientations, surface charge group densities, and electrolyte ionic strength. The numerical results are correlated with measured data[6] for two types of NW devices with and without gate oxides, respectively. In particular, the critical role of NW surface heterogeneity in determining the input dynamic ranges is investigated.

II. DEVICE PHYSIC AND MODELING APPROACH

A cross-sectional schematic plot of a NW biosensor immersed in an electrolyte solution is given in Fig. 1(a). Different layers are modeled, including the NW semiconductor, the gate oxide, the Stern layer, the biological membrane, and the electrolyte solution. In this numerical study, we assume cylindrical symmetry of the system and that the solution potential is defined by an immersed solution electrode. Nevertheless, our modeling approach readily applies to more gen-

[a]Electronic mail: yangliu@gloworm.stanford.edu.

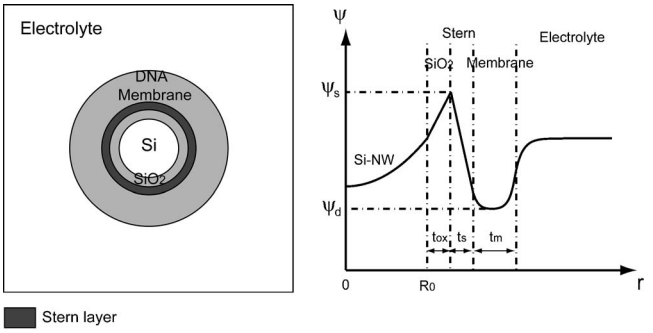

FIG. 1. (a) Schematic plot of a cross section of a Si-NW biosensor immersed in an electrolyte solution; (b) a typical electrostatic potential profile along the radial direction of a *p*-type Si-NW biosensor in the depletion mode, where ψ_s is the Stern layer surface potential and ψ_d the Donnan potential.

eral, two-dimensional cross sections and other biasing schemes. In the experiments,[3–7] the NWs typically operate in the accumulation mode or slightly in the depletion mode, where the electrical conduction is controlled by the majority carriers. Figure 1(b) shows a typical profile of electrostatic potential ψ along the radial direction of a *p*-type NW in the depletion mode. The spike at the interface between the oxide and the Stern layer is due to the positive charge associated with the surface charge groups. The potential approaches a constant, ψ_d, far inside the biological membrane, which is described by the Donnan equilibrium of the permeated electrolyte ions.[20,21,16] In the following, we present the physical models for the different layers of the biosensor system. The gradual channel approximation[22] is used to separate the variations in longitudinal (z-) and radial (r-) directions, which is applicable, considering that long NWs ($>\sim$micrometers) and small drain biases ($<\sim 100$ mV) are typically used.[6] Therefore, the modeling equations in the following should be regarded as applicable to one specific cross section; the longitudinal integration under a gradual channel approximation is further described toward the end of this section.

The semiconductor NW region is modeled by a nonlinear Poisson–Boltzmann-type equation for the electrostatic potential (ψ), holes (p), and electrons (n),

$$-\nabla\cdot(\varepsilon_{\mathrm{Si}}\nabla\psi)=q(p-n+N_{\mathrm{Dop}}),$$

$$p=n_i\exp[\beta(E_F+\Delta E_r-V_{\mathrm{GS}}-\psi)],$$

$$n=n_i\exp[\beta(-E_F-\Delta E_r+V_{\mathrm{GS}}+\psi)], \tag{1}$$

where q is the elementary charge, $\varepsilon_{\mathrm{Si}}$ the silicon permittivity, n_i the silicon intrinsic carrier density, N_{Dop} the net doping density in NWs, and E_F the carrier quasi-Fermi level. $\beta\equiv q/(kT)$ is defined, where k is the Boltzmann constant and T is the temperature. V_{GS} is the solution gate bias applied between the NW source electrode and the reference electrode immersed in the bulk electrolyte; the bulk electrolyte potential is set as the energy reference level, i.e., with the boundary condition $\psi|_{r\to\infty}=0$. ΔE_r is the reference energy difference between the solution gate electrode and the silicon region, accounting for the potential drop across the solution electrode and electrolyte interface as well as the affinity differences at oxide/electrolyte and oxide/silicon interfaces.[23] With all the interfacial potential discontinuities accounted for in ΔE_r, ψ is therefore continuous across the interfaces in our model. It was pointed out in Ref. 24 that the value of ΔE_r can be dependent on electrode/electrolyte surface adsorptions with platinum wire reference electrodes; the use of Ag/AgCl reference electrodes was recommended instead.

For the gate oxide region, the potential is modeled by Poisson's equation with the SiO_2 permittivity $\varepsilon_{\mathrm{ox}}$. The Stern layer is modeled as an additional dielectric layer between the oxide surface and the outer Helmholtz plane, as follows.[16] Its layer thickness (t_s) and permittivity (ε_s) are chosen so that its capacitance has the classical value of $\sim 20\ \mu\mathrm{F/cm^2}$. Poisson's equation is applied in that region

$$\nabla\cdot(\varepsilon_s\nabla\psi)+\sigma_s=0, \tag{2}$$

where σ_s is the surface charge density from the surface charge groups. It is known that amine groups may be introduced on functionalized NW surfaces besides the hydroxyl groups.[6,8] We consider contributions from both groups,

$$\sigma_s=q(N_hX_h+N_aX_a), \tag{3}$$

where N_h and N_a are the surface site densities of the hydroxyl and amine groups and X_h and X_a represent their average charges per site ($-1\leqslant X_h\leqslant 1$ and $0\leqslant X_a\leqslant 1$). The site binding models[17] are used to model the protonation and deprotonation processes of the two surface charge groups. The hydroxyl sites (S-OH) are amphoteric with reactions $\mathrm{S\text{-}OH_2^+}\leftrightarrow\mathrm{S\text{-}OH}+\mathrm{H^+}$ and $\mathrm{S\text{-}OH}\leftrightarrow\mathrm{S\text{-}O^-}+\mathrm{H^+}$; and the amine sites ($\mathrm{T\text{-}NH_2}$) are basic with a reaction $\mathrm{T\text{-}NH_3^+}\leftrightarrow\mathrm{T\text{-}NH_2}+\mathrm{H^+}$. By considering the balance between different charge states, we have as follows:[17]

$$X_h=\frac{(F_h^2-1)}{(F_h^2+\sqrt{K_h}F_h+1)} \tag{4}$$

for the hydroxyl sites, where K_h is defined as the ratio of the two reaction equilibrium constants and

$$X_a=\frac{F_a}{(F_a+1)} \tag{5}$$

for the amine sites. Here, two parameters have been defined to capture the Nernstian behavior of the site binding dynamics,

$$F_h=\exp[2.303(pI_h-pH)-\beta\psi_s] \tag{6}$$

and

$$F_a=\exp[2.303(pK_a-pH)-\beta\psi_s], \tag{7}$$

where pI_h is the isoelectric point of the hydroxyl group and pK_a is the dissociation constant of the amine group. It can be seen that surface charge (σ_s) and surface potential (ψ_s) affect each other in a self-consistent way. In general, the presence of surface charge groups contributes to the electrostatic screening of the biological charges and degrades NW sensing signals.

For the electrolyte solutions, the Poisson–Boltzmann model is used for the potential and ion distributions. In this work, we limit our scope to the common operational mode where a single reference electrode is used to define the potential of electrolyte solution under equilibrium. In the case of electrodiffusion, the more general Poisson–Nernst–Planck model would be needed.[14,15] The Poisson–Boltzmann equations for a monovalent salt are

$$-\nabla\cdot(\varepsilon_w\nabla\psi)=q(C_+-C_-),$$

$$C_+=C_0\exp(-\beta\psi),$$

$$C_-=C_0\exp(\beta\psi), \tag{8}$$

where ε_w is the water permittivity, C_+ and C_- are cation and anion densities, respectively, and C_0 is the buffer solution electrolyte concentration.

The surface immobilized DNA oligomers are modeled as an ion-permeable biological membrane layer with uniformly distributed biological charges, as follows.[16] The averaged charge density is calculated according to oligomer length, surface density, linear charge density [one electron per base for DNAs and neutral for peptide nucleic acids (PNAs)], and orientation. An extended Poisson–Boltzmann model is used for the biological membrane,

$$-\nabla\cdot(\varepsilon_m\nabla\psi)=q(C_+-C_-)+\rho_m,$$

$$C_+=C_0\exp[\beta(-\Delta G_m-\psi)],$$

$$C_-=C_0\exp[\beta(-\Delta G_m-\psi)], \tag{9}$$

where ε_m is the membrane permittivity and ρ_m is the biological charge density. The partition effect[18] is accounted for in this model, where ΔG_m is the free energy barrier that the mobile ions encounter as they permeate from the solution into the membrane. The Born charge-dielectric interaction energy is an important source of ΔG_m due to the permittivity difference between solution and membrane; the ion-solvent and ion-dipole interactions may also have significant contributions.[25] The modeling of the partition effect is important as some NW surface functionalization schemes may produce very densely immobilized oligomers.[6] Furthermore, the biological membrane will be packed even more densely in the case when the preferred DNA orientation is parallel to the NW surfaces.

In order to obtain the response curves of NW biosensors, it is essential to model the relation between the *c*-DNA concentration in solution (N_c) and the surface density of hybridized dsDNAs (N_{ds}). The basic Langmuir adsorption isotherm is usually used,[6,13]

$$N_{ds}=N_p\frac{K_cN_c}{K_cN_c+1}, \tag{10}$$

where N_p is the total surface density of primary DNAs for *c*-DNA binding and K_c is the *c*-DNA binding constant. However, the Langmuir isotherm is based on the assumption of a monolayer formation without biomolecule interactions or heterogeneity of the surface binding energies.[18] In practical situations, various extensions of the adsorption isotherm are often needed.[18,26,27] In this work, we consider the generalized Langmuir–Freundlich isotherm as follows:[26]

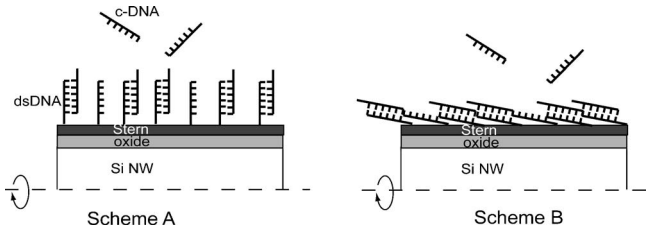

FIG. 2. Two orientation schemes of surface immobilized DNA oligomers used in the simulation study: (scheme A) the DNA oligomers are perpendicular to the NW surface; (scheme B) the DNA oligomers lie flat on the NW surface.

$$N_{ds}=N_p\frac{(K_cN_c)^v}{(K_cN_c)^v+1}, \tag{11}$$

where $0<v\leqslant 1$ is a parameter characterizing the heterogeneity of the surface binding energies. The heterogeneity can be due to the variations of biomolecule surface density and orientation distributions. The isotherm reduces to the Langmuir type in the special case of $v=1$.

The distributions of potential and charge carriers in both NWs and electrolyte are obtained by self-consistently solving the nonlinear model equations in the different regions [Eqs. (1), (2), (8), and (9)] for a quasi-Fermi level $E_F=E_F(z)$ at a particular cross section. The Newton iterative method is used to solve those coupled, nonlinear partial differential equations. The linear densities of NW electron and hole concentrations are then obtained as $\tilde{n}[E_F(z)]$ and $\tilde{p}[E_F(z)]$, respectively, by integrating n and p in the radial direction. Using the gradual channel approximation, the overall NW conductance is expressed as

$$G=I_{DS}/V_{DS}=\frac{q}{LV_{DS}}\int_0^{V_{DS}}[\mu_n\tilde{n}(E_F)+\mu_p\tilde{p}(E_F)]dE_F, \tag{12}$$

where μ_n and μ_p are the electron and hole mobilities, respectively. The integral can be readily evaluated numerically for a finite set of E_F points.

III. SIMULATION RESULTS AND DISCUSSIONS

By assuming cylindrical symmetry, we investigate two orientation schemes for the immobilized oligomers, as schematically shown in Fig. 2. In scheme A, the DNA strands are assumed to be perpendicular to the NW surface, while in scheme B they are assumed to be lying flat on the surface. From the electrostatic consideration,[28] scheme B is preferred for surfaces with positively charged amine groups. Nevertheless, we show results of both schemes for completeness. For scheme A, the membrane thickness is set to 5.5 nm, corresponding to the length of a 16-mer DNA strand. For scheme B, the membrane thickness is set to 2 nm.[16] In this study, we only consider the ion partition effect for scheme B, where the DNA strands are more densely packed. Table I summarizes the default values of important simulation parameters; those values are used throughout unless otherwise specified. Some

TABLE I. Symbols and default values of simulation parameters. The corresponding equations of their first appearance are also specified where applicable. The A and B labels in the parenthesis indicate which orientation scheme the value is used for.

Parameter	Symbol	Default value
NW radius	R_0	10 nm
NW length	L [Eq. (12)]	1 μm
NW drain voltage	V_{DS} [Eq. (12)]	50 mV
Solution gate voltage	V_{GS} [Eq. (1)]	0 V
Electrode reference energy difference	ΔE_r [Eq. (11)]	0.4 V
Oxide thickness	t_{ox}	1 nm
NW doping density	N_{dop} [Eq. (1)]	$10^{18}/\mathrm{cm}^3$, p-type
NW intrinsic carrier density	n_i [Eq. (1)]	$10^{10}/\mathrm{cm}^3$
NW electron mobility	μ_n [Eq. (12)]	400 $\mathrm{cm}^2/\mathrm{V\,s}$
NW hole mobility	μ_p [Eq. (12)]	60 $\mathrm{cm}^2/\mathrm{V\,s}$
Stern layer thickness	t_s	0.5 nm
Membrane thickness	t_m	5.5 nm (A); 2 nm (B)
Buffer solution ionic strength	C_0 [Eq. (8)]	100 mM
ssDNA length	L_{DNA}	16 bases
primary ssDNA surface density	N_p	$5\times10^{12}/\mathrm{cm}^2$
Vacuum permittivity	ε_0	8.85×10^{-14} F/cm^2
Silicon permittivity	ε_{Si} [Eq. (1)]	$11.9\varepsilon_0$
Oxide permittivity	ε_{ox}	$3.9\varepsilon_0$
Stern layer permittivity	ε_s [Eq. (2)]	$10\varepsilon_0$
Membrane permittivity	ε_m [Eq. (9)]	$80\varepsilon_0$ (A); $20\varepsilon_0$ (B)
Water permittivity	ε_w [Eq. (8)]	$80\varepsilon_0$
Hydroxyl surface density	N_h [Eq. (3)]	$1.5\times10^{14}/\mathrm{cm}^2$
Amine surface density	N_a [Eq. (3)]	$1.5\times10^{14}/\mathrm{cm}^2$
Buffer pH value	pH [Eq. (6)]	7
Hydroxyl isoelectric point	pI_h [Eq. (6)]	2
Hydroxyl rate constant ratio	K_h [Eq. (4)]	10^8
Amine acid dissociation constant	pK_a [Eq. (7)]	10
Partition free energy barrier	ΔG_m [Eq. (9)]	0 eV (A); 0.24 eV (B)
c-DNA binding constant	K_c [Eq. (10)]	$10^8/M$

of those parameter values are highly dependent on experimental conditions. The primary ssDNA surface density and c-DNA binding constants were reported to have values in the ranges of 10^{12}–$2.5\times10^{13}/\mathrm{cm}^2$ and 10^7–$5\times10^8/M$, respectively.[6,29] Their default values are here set to $5\times10^{12}/\mathrm{cm}^2$ and $10^8/M$, respectively. The hydroxyl group surface density is typically $5\times10^{14}/\mathrm{cm}^2$ for silicon dioxide surfaces without amine groups.[16] We assume a total surface charge group density of $3\times10^{14}/\mathrm{cm}^3$ to consider the possible bonding between DNAs and the amine groups as well as the steric effect. The partition free energy in the biological membrane is determined by complex processes, as mentioned in Sec. II. Its value in the case of DNA membrane is less characterized. Here, we simply consider the Born charge-dielectric interaction energy by assuming an ion radius of 2 Å. In the following simulations, we use a uniform grid spacing of 1 Å. By comparison with further simulations using finer grid spacing, the numerical error in the simulated potential profile is found to be less than 0.5 mV in all regions, and particularly less than 0.02 mV in the NW region.

Simulated I_d-V_g curves for a p-type NW biosensor are shown in Fig. 3; the simulations are conducted for NW surfaces without biomolecules, covered with primary ssDNAs, and covered with hybridized dsDNAs, respectively. The assumed DNA orientation scheme is B type. As the solution gate bias changes from −0.15 to 0.1 V, the Si-NW operation regime changes from accumulation to flatband and then to depletion mode. Upon the immobilization of the negatively charged primary ssDNAs, the corresponding voltage shift in the subthreshold regime (ΔV_0) is 42 mV. As the primary ssDNAs are fully hybridized, the membrane charge density doubles and the corresponding voltage shift (ΔV_{hyb}) is reduced to 5 mV. Such a reduction in the voltage shift is due to the nonlinearity of the electrolyte screening process and consistent with experimental observations.[6] For scheme A, the simulated ΔV_0 and ΔV_{hyb} are 7 and 5 mV, respectively (plots not shown). The relative conductance change, $\Delta G/G_{ss}$, is commonly used as the hybridization signal reading, where ΔG is the NW conductance change due to hybridization and G_{ss} is the conductance of the NW functionalized with primary ssDNAs. The dependence of $\Delta G/G_{ss}$ on the solution gate bias is given in the inset of Fig. 3. It is clearly shown that $\Delta G/G_{ss}$ is a sensitive function of the NW operation point in the accumulation, flatband or slightly depletion-mode regimes of operation. The curve saturates at its maximum value, $\exp(\beta\Delta V_{hyb})-1$, in the deep depletion regime. Therefore, we need to clearly account for the NW operation point when evaluating the relative conductance change. The depletion mode operation is indicated to be preferable for maximum sensing signals; nevertheless, noise constraints need to be considered in deep depletion mode when the NW current levels become very low.

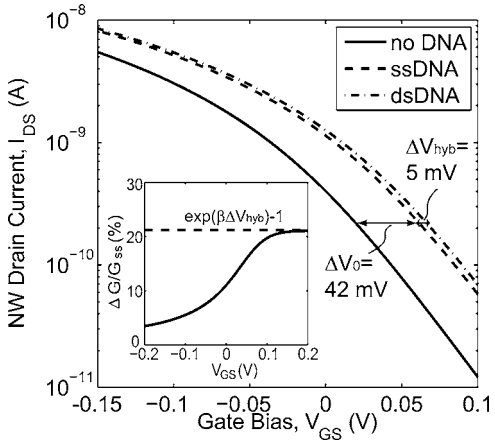

FIG. 3. Simulated I_d-V_g curves for a p-type Si-NW biosensor under conditions without DNA attachment, with primary ssDNAs, and with fully hybridized dsDNAs, respectively. The orientation scheme is B type. The inset shows the relative NW conductance change due to full hybridization of the primary ssDNAs as a function of the solution gate bias V_{GS}.

The simulated electrostatic potentials along the radial direction are plotted in Figs. 4(a) and 4(b) for the two DNA orientation schemes, respectively. At this particular operation point (V_{GS}=0 V), the NW region is depleted. Upon the immobilization of primary and complementary DNA oligomers, the NW potentials are lowered, consistent with the ΔV_0 and ΔV_{hyb} shifts in Fig. 3. It can be seen that for scheme A [Fig. 4(a)], the permeated ions reach an equilibrium with biological charge far inside the membrane; the potential approaches the constant Donnan potential,[20,21]

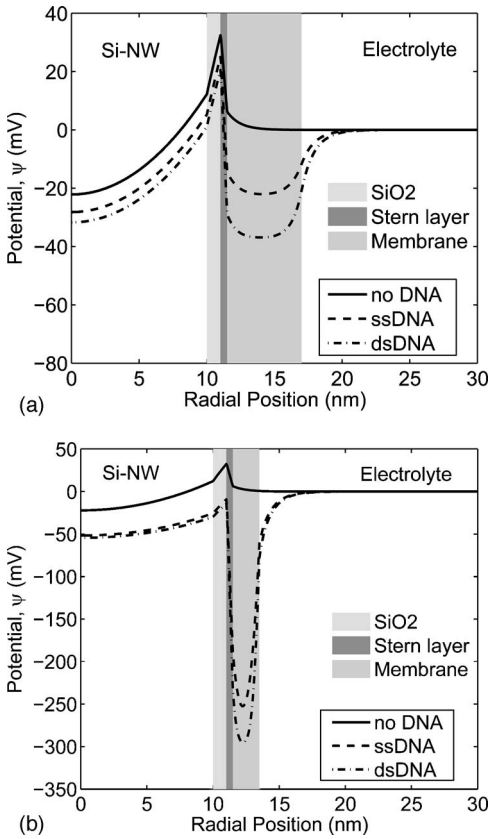

FIG. 4. Simulated radial potential distributions for the three NW surface conditions as in Fig. 3. Both DNA orientation schemes are examined: (a) scheme A and (b) scheme B.

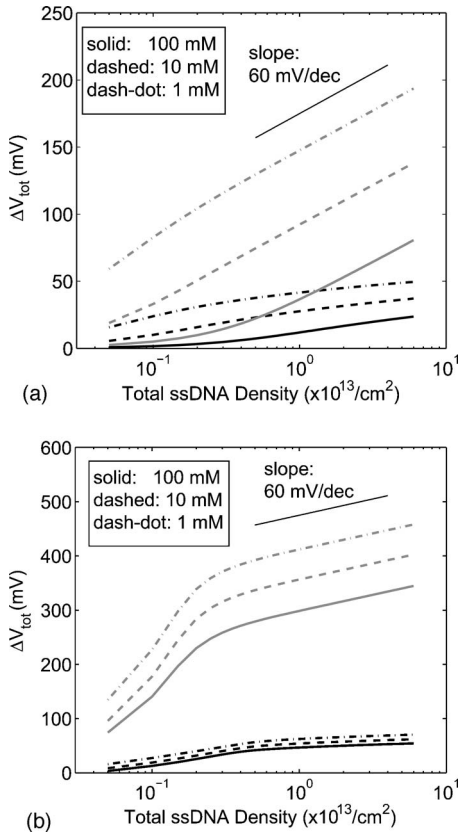

FIG. 5. Simulated total voltage shifts as functions of the total surface densities of immobilized ssDNAs including both primary and complementary species: (a) scheme A and (b) scheme B. Two surface charge group densities are examined: (black) high densities where $N_h=N_a=1.5\times10^{14}/\mathrm{cm}^2$ and (gray) low densities where $N_h=N_a=1.5\times10^{11}/\mathrm{cm}^2$. The three ionic strength conditions used in the simulations are 100, 10, and 1 mM, respectively.

$$\psi_D \equiv 1/\beta \sinh^{-1}[\rho_m/2qC_0'], \tag{13}$$

where $C_0' \equiv C_0 \exp(-\beta\Delta G_m)$ is the effective ionic strength inside the membrane with the partition energy accounted for. On the other hand, in the case of scheme B [Fig. 4(b)], the Donnan potential is not completely reached because the effective ionic strength is reduced with nontrivial ΔG_m. In the simulations, appreciable surface densities are used for the two surface charge groups ($1.5\times10^{14}/\mathrm{cm}^2$ for each group). At *p*H 7, the hydroxyl group charge is negative and the amine group charge positive; the overall net charge is positive, resulting in the positive spikes in the potentials at the oxide and Stern layer interface.

Figure 5 shows simulated total voltage shift (ΔV_{tot}) as a function of the total surface densities of the immobilized ssDNAs, including both primary and complementary species. Results for both orientation schemes are shown in Figs. 5(a) and 5(b), respectively. For each orientation scheme, different conditions are examined, including high and low surface charge group densities and three bulk electrolyte concentrations (C_0). As expected, ΔV_{tot} increases at lower ionic strength due to reduced electrolyte screening. We first look into the cases with low N_h and N_a so that the effect of surface charge groups is negligible. For scheme A, the Donnan equilibrium is reached inside the membrane and V_{tot} tracks the change of ψ_d.[16] As expected from Eq. (13), a 60 mV/decade dependence between ΔV_{tot} and $\ln(\rho_m)$ is observed in Fig. 5(a). This is also true for scheme B when the total ssDNA density is high enough so that the Donnan equilibrium is reached. However, at low ssDNA density in scheme B, the Donnan equilibrium is not reached; the electrolyte screening is instead governed by the Guoy–Chapman–Stern model. In the work of Ref. 13, the physical thicknesses of the biological membrane and the Stern layer were not considered; the biological charges were deposited exactly at the NW oxide surfaces. In that case, ΔV_{tot} would track the change of the surface potential $\psi_s \propto 2/\beta \ln(\rho_m)$, leading to an overestimated slope at 120 mV/decade.[20] In the case of high N_h and N_a, the effects of the surface charge groups are evident. They become more positively charged due to protonation upon DNA immobilization. The overall effect is the screening of the negative DNA charges and the suppression of the induced potential modulation, as manifested by the significantly reduced slopes for both orientations in Figs. 5(a) and 5(b).

In Fig. 6, we examine the dependence of ΔV_{hyb}, the voltage shift due to complete hybridization of the primary ssDNAs, on the surface densities of the primary ssDNAs (N_p) under the same simulation conditions as in Fig. 5. In the process of complete hybridization, the voltage shift is essentially induced by the doubling of the membrane charge density, i.e., $\Delta V_{\mathrm{hyb}}=\Delta V_{\mathrm{tot}}(2\rho_m)-\Delta V_{\mathrm{tot}}(\rho_m)$. In the case of low N_h and N_a, ΔV_{hyb} approaches asymptotically to a constant value, $\ln(2)/\beta \approx 18$ mV, as N_p increases for both schemes and all ionic strength conditions. This is a direct result of the 60 mV/decade dependence between ΔV_{tot} and biological

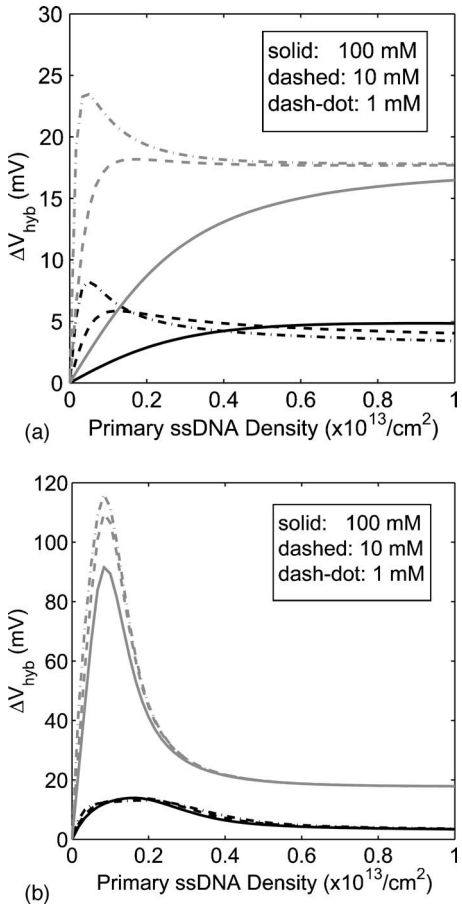

FIG. 6. Simulated voltage shifts from complete hybridization as functions of the primary ssDNA surface densities: (a) scheme A and (b) scheme B. Simulation conditions are the same as those used in Fig. 5: (black) high N_h and N_a and (gray) low N_h and N_a.

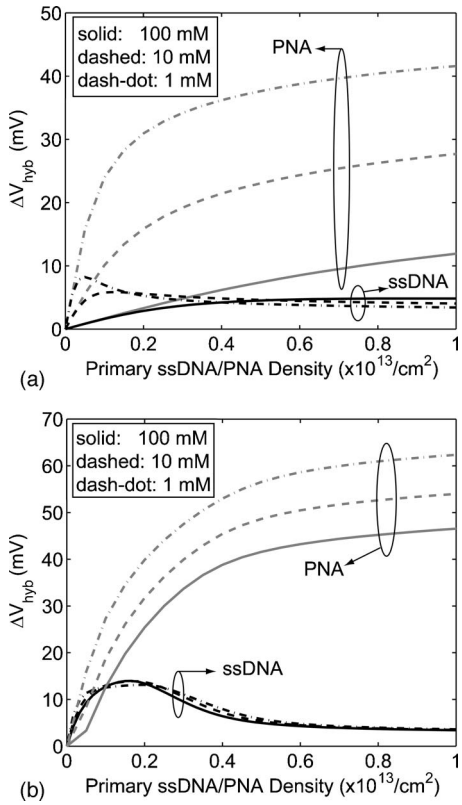

FIG. 7. Simulated voltage shifts from complete hybridization as functions of the primary oligomer densities for both orientation schemes: (a) scheme A and (b) scheme B. The primary receptors are assumed to be either PNAs (gray) or ssDNAs (black). Three ionic strength conditions are simulated at 100, 10, and 1 mM, respectively. The surface charge group densities are high throughout the simulations.

charge density as shown in Fig. 5. It is interesting to note that an optimal point of ΔV_{hyb} exists at low N_p for scheme A and 1 mM ionic strength, in agreement with the simulation results in Ref. 16. This is believed to be due to the transition from the Guoy–Chapman–Stern behavior at low N_p to the Donnan equilibrium at high N_p; such peaks are more evident for scheme B under all three ionic strength conditions. In the case of high N_h and N_a, ΔV_{hyb} is significantly reduced due to the protonation-induced charge screening effect. It is worth noting that at high N_p condition in the case of scheme A, enhanced ionic strength results in a slightly higher asymptotic ΔV_{hyb}. This counterintuitive behavior is explained by a higher order effect from the competition of electrolyte screening and surface charge group screening: the electrical double layer capacitance near the Stern layer surface increases at higher ionic strengths, which competes with surface group screening and forces the surface potential ψ_s to track ψ_d more closely.

Charge neutral PNA oligomers have been used replacing ssDNAs as the receptors,[3,7] mainly for the purpose of enhanced binding efficiency between PNAs and *c*-DNAs. We demonstrate that their charge neutral property also improves the transduction of the hybridization signals. Figure 7 shows the simulated ΔV_{hyb} as functions of primary oligomer densities for two cases with ssDNAs and PNAs as the receptors, respectively. It can be seen that for both orientation schemes and various ionic strength conditions, the PNA case generally leads to significantly enhanced signal levels compared to the ssDNA case. Such an improvement is explained by the nonlinear signal transduction behavior as shown in Fig. 5: the NW sensitivity degrades as their surfaces are more charged, which makes the use of neutral PNA receptors more favorable from signal transduction consideration.

The numerical model is applied to correlate with reported experimental data,[6] where detailed information on device parameters and characteristics was given. In their experimental work,[6] response curves were measured for two types of NW devices with or without the gate oxide layer, respectively. We adjust the simulation parameters according to the experimental characterization results. The *p*-type NW doping density was reported to be high $\sim 1\times 10^{19}/\text{cm}^3$ for the top few nanometers near the surface; but it decays rapidly farther inside the NWs.[30] We use a value of $4\times 10^{18}/\text{cm}^3$ in simulations. The buffer solution ionic strength is 165 mM. Based on a surface plasmon resonance measurement, the primary ssDNA surface density was found to be very high $(2.5\times 10^{13}/\text{cm}^2)$ for a poly-L-lysine-treated surface, while the value may be lower for the actual amine-terminated NW surfaces.[6] In our simulations, a value of $10^{13}/\text{cm}^2$ is used. Since the *p*H response indicated the amine group is dominant,[6] the amine group density is assigned with a value $(N_a = 1.5\times 10^{14}/\text{cm}^2)$ higher than that of the hydroxyl group

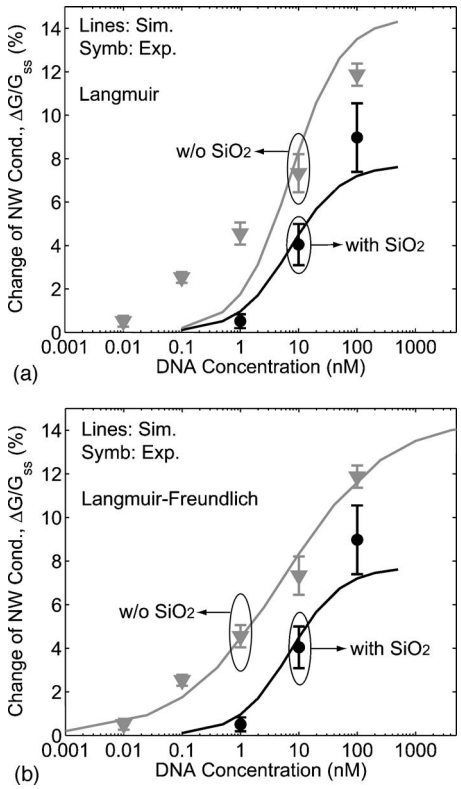

FIG. 8. Simulated and measured (Ref. 6) response curves for two types Si-NW devices with (black) or without (gray) the gate oxide layers: (a) the Langmuir isotherm is used; (b) the Langmuir–Freundlich isotherm is used, where $\upsilon=1$ for the device with the oxide and $\upsilon=1/2$ for the device without the oxide.

($N_h=0.75\times10^{14}/\mathrm{cm}^2$). Considering the high ssDNA density and positively charged NW surfaces, we assume the DNA orientation follows that of scheme B. We first examine the simulated response curves for the two cases (with or without oxide) using the basic Langmuir isotherm. In Fig. 8(a), it can be seen that the difference in the saturated signal levels (corresponding to complete hybridization) can be approximately accounted for by the presence or absence of the oxide layer. However, as for the input dynamic range, the simulations only match with the case with the oxide layer. In the case without the oxide layer, the measured input dynamic range is significantly increased by approximately two orders of magnitude, which cannot be explained by the simulations. Further simulations with different parameters produce different saturated signal levels; but the input dynamic range remains almost the same. In the work of Ref. 13, a simple, analytic model was proposed to explain the logarithmic response curves and the variations in input dynamic ranges. However, among other simplifications as discussed in previous sections, the simplified model[13] did not account for the charges of the primary ssDNAs. Even when the total voltage shift has a logarithmic dependence on the total biological charges, i.e., $\Delta V_{\mathrm{tot}}\propto\ln(\rho_m)$, the actual hybridization signal is $\Delta V_{\mathrm{hyb}}\propto\ln(1+\rho_{\text{c-DNA}}/\rho_p)$, where $\rho_{\text{c-DNA}}$ and ρ_p are the charge densities associated with immobilized c-DNAs and primary ssDNAs, respectively. In the limit of low analyte concentration, we would actually obtain a linear dependence between ΔV_{hyb} and the solution analyte concentration as long as the Langmuir isotherm is assumed. This is the underlying reason for the insensitivity of input dynamic range on the device parameters; the input dynamic range is mostly determined by the c-DNA binding dynamics. In Fig. 8(b), we consider the more general Langmuir–Freundlich isotherm, which accounts for the NW surface heterogeneity using a factor υ. The greatly enhanced input dynamic range in the case without the oxide layer is accounted for by assuming more heterogeneous binding energies ($\upsilon=1/2$). Considering the rather different chemical processes used in the two device types, such differences in the surface heterogeneity is very likely to occur even when they produce similar contact angles.[6] With this correlation study, we do not intend to exclude the applicability of other generalized adsorption isotherms. The strong indication here is that the complexity of the biomolecule binding dynamics may play a critical role in determining the input dynamic range, which may be further quantified with more detailed experimental characterization of the NW surfaces and biological membranes. It is an expected general effect that increased heterogeneity (smaller υ) produces a larger input dynamic range; this may be exploited for future designs of general affinity-type biosensors. Future model improvements in this direction need to be further enlightened by additional experimentation.

IV. CONCLUSIONS

We have developed a physical-based numerical model to simulate the device operation of Si-NW biosensors, where the ensemble of immobilized biomolecules are modeled as a charged, ion-permeable membrane with the partition effect considered. This model self-consistently accounts for surface-related physical and chemical processes that have a significant impact on the device performance, including transport of semiconductor carriers, electrolyte screening, protonation and deprotonation of surface charge groups, biomolecule surface binding dynamics, as well as the biomolecule surface orientations. Some important results from simulations with the model include (1) the relative NW conductance change depends on the choice of device operating point (i.e., depletion versus accumulation); (2) both the electrolyte mobile ions and the surface charge groups contribute to the nonlinear screening of the biological charges; (3) the use of charge neutral PNAs instead of ssDNAs as the receptors greatly improves the hybridization signal transduction; (4) the heterogeneity of the surface binding energies is critical in determining the biosensor input dynamic range as a result of correlation with experimental data for two types of devices with and without the oxide layer, respectively.

ACKNOWLEDGMENTS

We appreciate useful discussions with Dr. Clemens Heitzinger at University of Vienna on NW biosensors, in general.

[1] P. Bergveld, Sens. Actuators B **88**, 1 (2003).
[2] E. Souteyrand *et al.*, J. Phys. Chem. B **101**, 2980 (1997).
[3] J. Hahm and C. M. Lieber, Nano Lett. **4**, 51 (2004).
[4] Z. Li *et al.*, Nano Lett. **4**, 245 (2004).
[5] M. M.-C. Cheng *et al.*, Curr. Opin. Chem. Biol. **10**, 11 (2006).

[6]Y. L. Bunimovich *et al.*, J. Am. Chem. Soc. **128**, 16323 (2006).
[7]Z. Gao *et al.*, Anal. Chem. **79**, 3291 (2007).
[8]Y. Cui, Q. Wei, H. Park, and C. M. Lieber, Science **293**, 1289 (2001).
[9]G. Zheng, F. Patolsky, Y. Cui, W. U. Wang, and C. M. Lieber, Nat. Biotechnol. **23**, 1294 (2005).
[10]E. Stern *et al.*, Nature (London) **445**, 519 (2007).
[11]C. Heitzinger and G. Klimeck, J. Comput. Electron. **6**, 387 (2007).
[12]P. R. Nair and M. A. Alam, IEEE Trans. Electron Devices **54**, 3400 (2007).
[13]P. R. Nair and M. A. Alam, Nano Lett. **8**, 1281 (2008).
[14]Y. Liu, J. Sauer, and R. W. Dutton, J. Appl. Phys. **103**, 084701 (2008).
[15]Y. Liu, K. Lilja, C. Heitzinger, and R. W. Dutton, Tech. Dig. - Int. Electron Devices Meet. **2008**, 491.
[16]D. Landheer, G. Aers, W. R. McKinnon, M. J. Deen, and J. C. Ranuarez, J. Appl. Phys. **98**, 044701 (2005).
[17]D. L. Harame, L. J. Bousse, J. D. Shott, and J. D. Meindl, IEEE Trans. Electron Devices **ED-34**, 1700 (1987).
[18]A. J. Bard and L. R. Faulkner, *Electrochemical Methods: Fundamentals and Applications*, 2th ed. (Wiley, New York, 2001).
[19]Y. Liu and R. W. Dutton, *Transducers'09*, Denver, CO, 2009, p. 1678-1681.
[20]H. Ohshima, K. Makino, and T. Kondo, J. Colloid Interface Sci. **116**, 196 (1987).
[21]H. Ohshima and T. Kondo, J. Colloid Interface Sci. **123**, 136 (1988).
[22]Y. Taur and T. H. Ning, *Fundamental of Modern VLSI Devices* (Cambridge University Press, Cambridge, 1998).
[23]L. Bousse, J. Chem. Phys. **76**, 5128 (1982).
[24]E. D. Minot *et al.*, Appl. Phys. Lett. **91**, 093507 (2007).
[25]D. Deamer and A. Volkov, in *Permeability and Stability of Lipid Bilayers*, edited by E. A. Disalvo and S. A. Simon (CRC, Boca Raton, FL, 1995), Chap. 8, p. 161.
[26]R. Sips, J. Chem. Phys. **16**, 490 (1948).
[27]I. Quinones and G. Guiochon, J. Colloid Interface Sci. **183**, 57 (1996).
[28]A. Talasaz *et al.*, Proc. Natl. Acad. Sci. U.S.A. **103**, 14773 (2006).
[29]F. Yu, D. Yao, and W. Knoll, Nucleic Acids Res. **32**, 75 (2004).
[30]R. Beckman, E. Johnston-Halperin, Y. Luo, J. E. Green, and J. R. Heath, Science **310**, 465 (2005).